HHS Public Access

Author manuscript

Neuroimage. Author manuscript; available in PMC 2021 January 22.

Published in final edited form as:

Neuroimage. 2020 December ; 223: 117309. doi:10.1016/j.neuroimage.2020.117309.

Cortical iron disrupts functional connectivity networks supporting working memory performance in older adults

Valentinos Zachariou[a,1,*], **Christopher E. Bauer**[a,2], **Elayna R. Seago**[a,2], **Flavius D. Raslau**[b,2], **David K. Powell**[a,d,2], **Brian T. Gold**[a,c,d,1,*]

[a]Department of Neuroscience, College of Medicine, University of Kentucky, Lexington, KY 40536-0298 USA

[b]Department of Radiology, College of Medicine, University of Kentucky, Lexington, KY 40536-0298 USA

[c]Sanders-Brown Center on Aging, College of Medicine, University of Kentucky, Lexington, KY 40536-0298 USA

[d]Magnetic Resonance Imaging and Spectroscopy Center, College of Medicine, University of Kentucky, Lexington, KY 40536-0298 USA

Abstract

Excessive brain iron negatively affects working memory and related processes but the impact of cortical iron on task-relevant, cortical brain networks is unknown. We hypothesized that high cortical iron concentration may disrupt functional circuitry within cortical networks supporting working memory performance. Fifty-five healthy older adults completed an N-Back working memory paradigm while functional magnetic resonance imaging (fMRI) was performed. Participants also underwent quantitative susceptibility mapping (QSM) imaging for assessment of non-heme brain iron concentration. Additionally, pseudo continuous arterial spin labeling scans were obtained to control for potential contributions of cerebral blood volume and structural brain images were used to control for contributions of brain volume. Task performance was positively correlated with strength of task-based functional connectivity (tFC) between brain regions of the frontoparietal working memory network. However, higher cortical iron concentration was associated with lower tFC within this frontoparietal network and with poorer working memory performance after controlling for both cerebral blood flow and brain volume Our results suggest

*Correspondence author. vzachari@uky.edu (V. Zachariou), brian.gold@uky.edu (B.T. Gold).

[1]Contributed to the design of the experiment, the collection and analyses of the data, and writing the manuscript.

[2]Contributed to the analyses of the data and writing the manuscript.

CRediT authorship contribution statement

Valentinos Zachariou: Conceptualization, Methodology, Software, Formal analysis, Data curation, Writing - original draft, Writing - review & editing, Visualization. **Christopher E. Bauer:** Methodology, Formal analysis, Data curation, Investigation, Writing - review & editing. **Elayna R. Seago:** Formal analysis, Data curation, Visualization. **Flavius D. Raslau:** Resources, Data curation. **David K. Powell:** Formal analysis, Data curation, Writing - review & editing. **Brian T. Gold:** Conceptualization, Methodology, Data curation, Writing - review & editing, Visualization, Supervision, Project administration, Funding acquisition.

Declaration of Competing Interest

The authors declare no competing financial interests.

Supplementary materials

Supplementary material associated with this article can be found, in the online version, at doi:10.1016/j.neuroimage.2020.117309.

that high cortical iron concentration disrupts communication within frontoparietal networks supporting working memory and is associated with reduced working memory performance in older adults.

Keywords

Aging; Brain; Working memory; QSM

1. Introduction

Non-heme iron is crucial for many cellular processes including adenosine triphosphate (ATP) generation in mitochondria, neurotransmitter synthesis and myelin generation (Mills et al., 2010; Todorich et al., 2009; Raz and Daugherty 2018). However, non-heme iron is a potent oxidizer that can contribute to oxidative stress, interfere with neurotransmission and lead to cell death (Zecca et al., 2004; Moos et al., 2007; Ke and Qian, 2007; Becerril-Ortega et al., 2014; Hare and Double, 2016; Matak et al., 2016). Thus, non-heme iron is typically sequestered in iron storage complexes such as ferritin, which release it in a tightly regulated manner (Hentze, Muckenthaler and Andrews, 2004; Moos et al., 2007).

Normal aging perturbs the iron sequestration process, leading to non-heme iron accumulation outside of storage complexes (Lauffer, 1992; Wayne Martin et al., 1998; Zecca et al., 2004). Age related increases in non-heme brain iron have been repeatedly linked with poorer working memory performance (cross-sectional: Bartzokis et al., 2011; Darki et al., 2016; longitudinal: Daugherty, Haacke and Raz, 2015) as well as declines in other cognitive and motor domains (cross-sectional: Sullivan et al., 2009; Penke et al., 2012; Rodrigue et al., 2012; Ayton et al., 2017). Further, longitudinal brain iron accumulation has also been linked with corresponding declines in brain structural volumes. A specific pattern that has been reported in recent studies has been that age-related iron accumulation in the basal ganglia and hippocampus predict subsequent atrophy in these structures and corresponding cognitive declines (e.g. Daugherty, Haacke and Raz, 2015; Daugherty and Raz, 2016).

Interestingly, relationships between regional brain iron concentrations and performance (e.g. general cognitive ability, working memory, episodic memory and motor performance) have been reported even when no relationships are detected between iron and regional brain volumes (Sullivan et al., 2009; Penke et al., 2012; Kim et al., 2017; Van Bergen et al., 2018; Acosta-Cabronero et al., 2018). Together, this pattern of results suggests that some iron-mediated cognitive alterations may relate to disruption of functional brain systems that are not directly related to changes in brain volume. Consistent with this possibility, results from recent studies have shown that striatal iron concentration is negatively associated with BOLD magnitude (Kalpouzos et al., 2017), BOLD modulation (Rodrigue et al., 2020) and reduced resting-state functional coherence between striatal networks and the rest of the brain (Salami et al., 2018) but not with corresponding structural volume (both Kalpouzos et al., 2017; Salami et al., 2018).

However, the impact of *cortical iron* on brain networks directly supporting cognitive task performance remains unknown. Based on previous literature focused on striatal iron content

(Rodrigue et al., 2020; Salami et al., 2018), we hypothesized that excessive brain iron may disrupt large-scale functional networks directly supporting task performance in older adults. More specifically, we would expect excessive iron to disrupt functional connectivity within task-relevant networks because (1) excessive iron is known to interfere with proper neurotransmission (Zecca et al., 2004; Becerril-Ortega et al., 2014), which is required to support functional connectivity of large scale brain networks (Duncan et al., 2013; Kapogiannis et al., 2013) and (2) age-related cognitive declines tend to progress along connected brain networks (Greicius and Kimmel, 2012; Damoiseaux et al., 2012; Damoiseaux 2017).

Here, we explored this possibility by evaluating the impact of cortical iron concentration on neighboring cortical functional-connectivity brain networks directly supporting working memory performance in older adults. The cognitive domain of working memory was selected due to the established negative association between brain iron concentration and working memory performance (Bartzokis et al., 2011; Daugherty, Haacke and Raz, 2015; Darki et al., 2016). Working memory is also of functional relevance in that it declines significantly with aging and is considered a contributing source of other age-related cognitive deficits including long-term memory, decision making and problem solving (Zacks et al., 2000; Park and Hedden 2001; Reuter-Lorenz and Sylvester, 2005; Glisky, 2007; Blacker et al., 2007; Belleville et al., 2008).

Participants completed an N-Back working memory paradigm while functional magnetic resonance imaging (fMRI) was performed and also received a separate QSM scan (Wang and Liu, 2015; Wang et al., 2017) for estimation of non-heme brain iron concentration. QSM capitalizes on the fact that paramagnetic iron is the dominant source of magnetic susceptibility in gray matter, augmenting the magnetic field in a roughly linear manner and yielding iron estimates highly correlated with postmortem tissue iron concentrations (Langkammer et al., 2012; Sun et al., 2015; Hametner et al. 2018; Fukunaga et al. 2010). Importantly, QSM is sensitive to non-heme iron concentrations in both cortical gray matter regions (Fukunaga et al. 2010; Liu et al. 2012; Hametner et al. 2018; Kagerer et al. 2020) and subcortical structures (Li et al., 2014; Ayton et al., 2017; Van Bergen et al., 2018).

However, the QSM signal is not specific to non-heme iron. In particular, heme iron (which binds oxygen to hemoglobin in blood) can contribute to the QSM signal in its deoxygenated state. To control for contributions of cerebral blood volume to the QSM signal, pseudo continuous arterial spin labeling (PCASL) scans were obtained and CBF was included as a covariate in QSM-related analyses. Further, to control for potential structural contributions to our QSM-function relationships, structural volume was added as a covariate in QSM-analyses.

2. Materials and Methods

2.1. Participants

Fifty-six healthy older adults were recruited for the experiment (31 women, age range 61–86 years). All participants provided informed consent under a protocol approved by the Institutional Review Board of the University of Kentucky. Participants were recruited from

an existing longitudinal cohort at the Sanders-Brown Center on Aging (Schmitt et al., 2012) and the Lexington community. All participants were cognitively intact based on clinical consensus diagnosis and scores from the Uniform Data Set (UDS2) used by US ADCs (procedure outlined in Morris et al., 2006) or a score of 26 or higher on the Montreal Cognitive Assessment (MoCA; Nasreddine et al., 2005). The UDS2 includes a comprehensive battery of neuropsychological tests assessing global cognition, memory encoding, memory retrieval, semantic memory, working memory, attention, executive function, processing speed, and verbal retrieval.

Exclusion criteria were significant head injury (defined as loss of consciousness for more than five minutes), heart disease, neurological or psychiatric disorders, claustrophobia, pacemakers, the presence of metal fragments or any metal implants that are incompatible with MRI, diseases affecting the blood (anemia, kidney/heart disease etc.) or significant brain abnormalities detected during imaging. A neuroradiologist (F.D.R.) evaluated the T1W and FLAIR images for evidence of stroke or other abnormalities. One participant was excluded from the sample due to the presence of an old stroke within the right motor cortex. Detailed characteristics of the final group of participants are shown in Table 1.

Table 1. Group demographics and mean cognitive measures. The table lists the total number of participants, mean (± sd) for age, male/female distribution, years of education, Mini-Mental State Exam (MMSE) and Montreal Cognitive Assessment (MoCA) scores.

2.2. Task Design

Participants performed a visual working memory paradigm (N-Back task; adapted from Hakun and Johnson, 2017), comprised of three task conditions: a control condition (Compare), a 1-Back condition and a 2-Back condition within the context of a blocked design (Fig. 1). Task stimuli consisted of eight consonant letters, presented in black, at the center of the display, against a white background. For each condition, stimulus/trial duration was 2 s and trials were separated by 500 ms of fixation.

The experiment was divided into two 240 s fMRI runs. Each run consisted of three task blocks (one of each condition) with fifteen trials each (30 trials per condition total) and four fixation blocks (visual baseline). Each task block lasted 40 s and each fixation block lasted 30 s. During the Compare condition, participants indicated whether two (randomly selected) letters presented side-by-side were the same or different via button presses. In seven out of the fifteen trials of the Compare condition, the letters matched. During the 1-Back condition, participants were asked to judge whether the letter on the current trial matches the one presented immediately prior to the present letter. During the 2-Back condition, participants decided if the letter on the current trial matches with the one presented two items prior to the present letter. For the 1-Back and 2-Back conditions, four out of the fifteen trials of this task (randomly selected) comprised a match. Responses were made using MRI compatible response buttons (one in each hand). Participants were asked to press the right button for “same” judgments and press the left button for “different” judgments. Participants were asked to respond as quickly and accurately as possible and completed a brief practice session on the N-Back task prior to entering the MRI scanner.

The experiment, implemented in E-prime 3.0, was run on a Windows-10 based PC. Stimuli were presented via an analog projector on a 200 × 100 mm^2 screen (visual angle: 20° horizontal x 10° vertical), mounted 550 mm away from the participants' eyes and situated at the bore opening of the MRI scanner. The experiment was presented at a resolution of 1280 × 1024 pixels and participants viewed the projection screen via a mirror attached to the head coil of the scanner.

2.3. Behavioral Data Analyses

Behavioral data collected during the scans were first imported to Excel in order to calculate D-prime (Stanislaw and Todorov, 1999) for each of the N-Back task conditions. D-prime was log transformed in all analyses involving MRI-based measures under the assumption that large differences in D-prime are typically associated with smaller differences in MRI-based measures. Log D-prime was then used in SPSS to conduct subsequent ANOVAs and linear regression analyses in conjunction with the QSM and tFC measures of interest.

2.4. Imaging Protocol

Participants were scanned with a Siemens 3T PRISMA Fit scanner (software ver. E11C), using a 64-channel head-coil, at the University of Kentucky Magnetic Resonance Imaging and Spectroscopy Center (MRISC). The following sequences were collected: 1) a high resolution, multi-echo, T1-weighted anatomical image (MEMPR); 2) two fMRI T2* runs, 3) double-echo gradient echo field map images for spatial distortion correction of the fMRI data; 4) a high-resolution, flow compensated, multi-echo, 3D spoiled GRE sequence for Quantitative Susceptibility Mapping (QSM); and 5) a Pseudo Continuous Arterial Spin Labelling (PCASL) perfusion image (3D-GRASE acquisition with background suppression). Several other sequences were collected during the scanning session related to other scientific questions and are not discussed further here.

The MEMPR sequence had four echoes [repetition time (TR) = 2530 ms; first echo time (TE1) = 1.69 ms echo time spacing (ΔTE) = 1.86 ms, flip angle (FA) = 7°] and covered the entire brain [176 slices, field of view = 256 mm, parallel imaging (GRAPPA), acceleration factor = 2, 1 mm isotropic voxels, scan duration = 5.53 min]. The MEMPR sequence was used to optimize the Freesurfer cortical segmentation and improve the accuracy of the gray matter lobar masks (Van der Kouwe et al., 2008). The two fMRI runs were acquired with an echo-planar imaging sequence (EPI; TR = 2500ms, TE = 30ms, flip angle = 90°, resolution = 3.0 mm isotropic voxels, 64 × 64 matrix, field of view = 192 mm, 40 axial slices covering the whole brain). The GRE field map scan was acquired right after the second EPI sequence at the same resolution, field of view and number of axial slices as the EPI sequences. A high-resolution, flow compensated, multi-echo, 3D spoiled GRE sequence in the sagittal plane with eight echoes (TR/TE1/ΔTE/FA = 24ms/2.98ms/2.53ms/15°) was acquired and used to create QSM images. The entire brain was covered [acquisition matrix = 224 × 224 × 144, parallel imaging (GRAPPA) acceleration = 2, 1.2 mm isotropic voxels and scan duration = 6.18 min]. The PCASL sequence parameters were as follows: 36 slices, resolution = 3.4 × 3.4 × 4.0 mm, FOV = 220 mm, TR = 5070 ms, inflow time = 4.525 s, labelling duration = 2.025 s, nine tagged-untagged pairs and a single T1-corrected, M_0 calibration image for CBF quantification and scan duration = 5.09 min].

2.5. fMRI Pre-processing

Functional scans were first corrected for field inhomogeneity induced geometric distortions using FUGUE (https://fsl.fmrib.ox.ac.uk/fsl/fslwiki/FUGUE) and the GRE field map data in FSL (Jenkinson et al., 2012; Smith et al., 2004). Subsequently the functional scans were motion corrected and/or despiked where necessary (https://afni.nimh.nih.gov/pub/dist/doc/program_help/3dDespike.html), co-registered to their contrast-corrected (using Siemens Prescan Normalize option) anatomical image (after averaging the four echoes of the MEMPR into a single root mean square image), warped to MNI space, using the MNI ICBM152, 1mm, 6^{th} generation atlas (Grabner et al., 2006) and a non-linear transformation (3dQwarp; https://afni.nimh.nih.gov/pub/dist/doc/program_help/3dQwarp.html), smoothed with a Gaussian kernel of 6.0 mm FWHM and mean-based intensity normalized (all volumes by the same factor) using AFNI (Cox 1996). In addition, linear and non-linear trends (where necessary) were removed during pre-processing of the data and motion parameters were regressed separately for each run from all analyses. Lastly, all TR pairs in which the Euclidean Norm of the motion derivative exceeded 0.3 (the AFNI default for adults) were censored and removed from the analyses.

2.6. fMRI Analyses

Group-level, whole brain contrasts between N-back conditions were performed to identify the broad working memory network and to delineate seeds for subsequent functional connectivity analyses. The Group level analysis of the N-Back task was conducted using AFNI (Cox 1996) and a linear mixed effects model (3dLME; Chen et al., 2013) with participant age added as a covariate. The resulting statistical maps were adjusted for multiple comparisons using the false discovery rate approach at qFDR < 0.01. The functional contrast of 2-Back/2 + 1-Back/2 > Compare was used to identify brain regions in which activity for the N-Back task was greater than that of the visual control task.

2.7. Functional Connectivity Preprocessing

Additional pre-processing steps were performed prior to the functional connectivity analysis, according to the basic ANATI-COR regression-based approach (e.g. Jo et al., 2010; Gotts et al., 2012; Stoddard et al., 2016). Using each participant's anatomical scan (root mean square MEMPR), segmented ventricular, gray and white matter masks were created (using SPM12; http://www.fil.ion.ucl.ac.uk/spm/software/spm12/), for each participant. All masks were resampled to the EPI voxel resolution, and ventricle and white matter masks were eroded by one voxel (or by two voxels if we observed task-like components in the first three principal components of the PCA analysis described below) to prevent partial volume effects with gray matter.

Separate nuisance time series were then extracted for ventricles and white matter. In total, the nuisance regression for each participant comprised 11 regressors of no interest: six motion parameters, one average ventricle time series, one localized estimate of white matter (averaging within a sphere of radius 20 mm centered on each voxel), and the first three principal components of all voxel time series from a combined ventricle and white matter mask, calculated after first detrending with AFNI's second-order polynomial baseline model (Stoddard et al., 2016; comparable to aCompCor in Behzadi et al., 2007). After this nuisance

model was subtracted from each participant's EPI data to obtain the cleaned residual time series, a task regression was performed to further remove any evoked responses from the blocks during the task (using the BLOCK model in AFNI's 3dDeconvolve). The resulting time series were then extracted separately from blocks of different conditions, with blocks of the same type concatenated together for purposes of condition comparisons after adjusting for the delay in the BOLD signal in each block (6 s after the start of each block to 4 s after the end). Estimates of the level of residual global artifacts present in the residual time series (which include factors like head motion, cardiac and respiration effects, etc.) were calculated per condition for later use as nuisance covariates in group-level analyses using the global level of correlation or "GCOR" (e.g. Gotts et al., 2013; Saad et al., 2013), which is the grand average correlation of all gray matter voxels with each other.

2.8. Functional Connectivity Analyses

All positively activated regions from the fMRI, group-level functional contrast of 2-Back/2 + 1-Back/2 > Compare were used as seed regions of interest (ROIs) for the functional connectivity analyses which was conducted as follows: first, a numbered mask was created using all the seed ROIs with the voxels of each ROI in the mask assigned a different positive integer value. Then, using this mask and the cleaned residual time series in all gray matter voxels (described in the functional connectivity pre-processing section), we calculated a correlation matrix comprised of Pearsons's r values and their corresponding Fisher-Z transform (see 3dNetCorr; Taylor and Saad, 2013) for the set of seed ROIs included in the mask, separately for each N-Back task condition (1-Back, 2-Back and Compare). Then for each participant, we subtracted the Compare correlation matrix from the average of the N-Back task matrices, as in the contrast of 2-Back/2 + 1-Back/2 > Compare used in the fMRI group level analysis previously. This resulted in a new correlation matrix corresponding to the task-based functional connectivity between all seed ROIs. This new matrix was used to calculate average task-based functional connectivity (tFC) of each seed ROI with every other ROI (one average tFC value per seed ROI per participant), using the Fischer-Z transformed values (which yields normally distributed values). These, per seed, average connectivity values were then used in subsequent linear regression analyses in SPSS with age, gender and GCOR (described in the functional connectivity pre-processing section; see also Gotts et al., 2013) added as nuisance covariates to these condition comparisons.

2.9. Volumetric Analyses

Freesurfer 6.0 was used with the recon-all option (all available parcellations) to segment each participant's MEMPR scan. Next, lobar cortical gray matter (GM) masks were created as recommended by Freesurfer (https://surfer.nmr.mgh.harvard.edu/fswiki/CorticalParcellation) by joining together the relevant GM (cortical only) segmented structures/masks associated with each of the four lobes. Masks of the caudate and putamen were also created from the corresponding Freesurfer segmented structures of the basal ganglia. The volume (in mm^3) of these GM masks and the Freesurfer estimated intracranial volume (eICV, in mm^3), were recorded for each participant for use in subsequent volumetric analyses. The same Freesurfer-derived cortical and subcortical masks used to extract volumetric data were also used to extract QSM and CBF values for the analyses described below.

2.10. Quantitative Susceptibility Mapping (QSM) Processing

GRE images were processed in MATLAB using the Morphology Enabled Dipole Inversion toolbox (MEDI toolbox, release of 11/06/2017; J. Liu et al., 2012; Liu et al., 2011a, 2011b; T. Liu et al., 2012). This approach generates QSM images by inverting an estimate of the magnetic field that is structurally consistent with anatomy in order to generate a distribution of local magnetic susceptibility values. The required scans for the MEDI analyses are a phase image and a skull-stripped (using BET; Smith, 2002) magnitude image obtained during the same scan.

The following steps were performed during MEDI: 1) non-linear fitting to the multi-echo data was used to estimate the magnetic field inhomogeneity. 2) Phase unwrapping using the magnitude image as a guide (Liu et al., 2013). 3) Removal of the background field by applying a projection onto the dipole field (see Liu, Khalidov et al., 2011). 4) The remaining field was inverted to calculate the quantitative susceptibility map. Lastly 5) local magnetic susceptibility within cerebrospinal fluid (CSF; specifically within the lateral ventricles) was used to scale the QSM maps such that positive values corresponded to local magnetic susceptibility greater than that of CSF and negative values corresponded to local magnetic susceptibility less than that of CSF. CSF within the lateral ventricles was selected as the reference for the QSM analyses because CSF susceptibility is fairly uniform and does not scale with participant demographic variables such as age and gender.

For this reference step, ventricular masks were created separately for each participant as follows: The MEMPR was first registered to the GRE magnitude image using the AFNI function align_epi_anat.py (https://afni.nimh.nih.gov/pub/dist/doc/program_help/align_epi_anat.py.html). Then using this magnitude aligned MEMPR scan in conjunction with ALVIN (see Kempton et al., 2011; https://sites.google.com/site/mrilateralventricle/) and SPM12, lateral ventricle masks were created for each participant. These masks were then eroded by one voxel to prevent partial volume effects with the surrounding subcortical gray and white matter, resampled to the QSM voxel resolution (1.2 mm isotropic), visually inspected for correctness while overlaid on both the GRE magnitude image and the aligned MEMPR image, and used in the MEDI toolbox as the CSF reference mask for each participant.

2.11. GM Masks for QSM

The same Freesurfer-derived cortical and subcortical GM lobar masks used to extract volumetric data were used to extract QSM data. This approach was adopted due to superior registration associated with the use of masks generated on each participant's own individual morphology in native space, allowing for extraction of volumetric and QSM values in the same cortical structures (Fig. 2). The following steps were used to register participants' Freesurfer derived masks to their QSM images in native space: each participant's high-resolution MEMPR was aligned to their high-resolution QSM magnitude image using the AFNI align_epi_anat.py function and a local Pearson correlation cost function. The resulting transformation matrices were then applied to each participants' Freesurfer masks using the AFNI function 3dAllineate (https://afni.nimh.nih.gov/pub/dist/doc/program_help/3dAllineate.html) with a nearest neighbor interpolation method. Lastly, each mask was

eroded by one voxel to prevent partial volume effects and then resampled to the QSM voxel resolution (i.e. from 1 mm isotropic to 1.2 mm isotropic voxels).

Values from QSM maps were then extracted from each of the magnitude-aligned, resampled and eroded GM masks for each participant. Only positive QSM values (susceptibility greater than that of CSF in the lateral ventricles) were extracted in order to limit QSM signal from myelin, associated with bordering white matter and neuropil, which has negative QSM values relative to CSF due to the diamagnetic effect of myelin on susceptibility (e.g. Wisnieff et al., 2015; Hametner et al., 2018). Our rationale for use of positive voxels only is that this study focused on the effects of iron concentration, as opposed to myelin concentration, on cognition and functional connectivity.

To confirm that negative voxels in cortical GM represent QSM signal from myelin, we performed secondary analyses using white matter (WM) as our reference region (instead of CSF). If myelin is the major source of negative QSM signal in our data then voxels in our gray matter ROIs (which contained a mixture of positive and negative values when referenced to CSF) should only have positive values when referenced to WM. This is exactly what we found. With WM as the reference, all voxels in cortical GM were positive (Supplementary Figure 1). However, because myelination varies between people, QSM values scaled to myelin do not correlate with age in any of the cortical ROIs. Given that iron is well-established to track with age, we opted to use CSF as the reference instead of WM and exclude negative voxels reflecting high myelin concentrations. Results from voxelwise analyses using this approach demonstrated robust QSM signal in cortex, particularly within motor cortex, a region known to accumulate significant iron with age (Supplementary Figure 2).

Normalized lobar QSM values were then created for each participant by dividing the sum of positive QSM values from each mask by the total number of voxels of their corresponding GM mask, resulting in a final unit measure of iron concentration in parts per billion by mm^3 (ppb/mm^3).

2.12. Pseudo Continuous Arterial Spin Labelling (PCASL) processing

PCASL scans were processed in FSL (Jenkinson et al., 2012; Smith et al., 2004) using the following procedure: first, all tagged/untagged pairs were motion corrected to the M_0 image using FSL MCFLIRT. A perfusion image was subsequently created using asl_file (https://fsl.fmrib.ox.ac.uk/fsl/fslwiki/asl_file/Tutorial) by calculating the mean difference between the tagged and untagged pairs. Oxford_asl (https://fsl.fmrib.ox.ac.uk/fsl/fslwiki/oxford_asl) was then used with a per-voxel calibration method, (using the M_0 image) to create a calibrated map of resting state tissue perfusion in absolute units (ml/100 g/min).

2.13. GM Masks for PCASL

The same Freesurfer-derived GM masks used to extract volumetric data and QSM data were used to extract PCASL data. Each participant's high-resolution MEMPR was aligned to their PCASL M_0 image using the AFNI align_epi_anat.py function and a local Pearson correlation cost function. The resulting transformation matrices were then applied to each participants' Freesurfer masks using the AFNI function 3dAllineate with a nearest neighbor

interpolation method. Lastly, each mask was eroded by one voxel to prevent partial volume effects and resampled to the PCASL voxel resolution (i.e. from 1 mm isotropic to 3.4 mm isotropic voxels).

Average CBF values from the calibrated perfusion maps were then extracted using each of the M_0 aligned, resampled and eroded GM masks for each participant. A total cortical CBF mask, comprised by the individual lobar cortical masks, was also used to extract total cortical CBF values. Similarly a CBF mask comprised by the caudate and putamen masks was used to extract total CBF values from these striatal regions. Total cortical, striatal, or specific lobar cortical CBF, values were used as covariates in all QSM analyses as appropriate to account for differences across participants in cerebral blood volume.

2.14. QSM within the tFC Seed ROIs

To evaluate the concentration of iron within the tFC ROIs the following steps were performed: first, each participants' QSM magnitude-image-aligned MEMPR was warped to MNI space, using the MNI ICBM152, 1mm, 6th generation atlas (Grabner et al., 2006) and a non-linear transformation (3dQwarp; https://afni.nimh.nih.gov/pub/dist/doc/program_help/3dQwarp.html). The inverse transformation matrix was then applied to each tFC seed ROI from MNI space back to each participant's native space using the AFNI function 3dNwarpApply (https://afni.nimh.nih.gov/pub/dist/doc/program_help/3dNwarpApply.html) and a nearest neighbor cost function and then resampled to the QSM voxel resolution. Values from QSM maps were extracted from each of these resampled tFC ROIs for each participant, using only positive QSM values (referred to as pQSM in the results section) in order to avoid contamination from myelin signal (as discussed in the QSM lobar ROI section).

Normalized QSM tFC seed ROI values were then created by dividing the sum of positive QSM values in each participant's tFC ROI by the total number of voxels in their corresponding tFC ROI mask, resulting in a final unit measure of iron concentration in parts per billion by mm^3 (ppb/mm^3). QSM values from these seed ROIs were used in subsequent analyses to evaluate differences in iron concentration between the tFC seeds.

2.15. Statistical Analyses

Statistical analyses were performed using SPSS 24 (IBM, Chicago, IL, USA). The main analyses involved independent sample t-tests (2-tailed), repeated measures ANOVAs, bootstrapped (10,000 samples) univariate and multivariate ANOVAs and linear regression models with bias-corrected accelerated (BCa) 95% confidence intervals (CI). In all analyses, gender and age were added as covariates. GCOR (described in the functional connectivity pre-processing section) was used as an additional covariate in all regression models in which tFC measures were used. Cortical/striatal GM CBF values, or specific lobar GM CBF (e.g. parietal CBF) values were used as covariates in QSM analyses as appropriate. eICV (described in volumetric analysis section) was used as a covariate in all volumetric analyses and was also used to create adjusted measures of cortical (total and/or individual lobe) GM volumes, using the residualization approach (Sanfilipo et al., 2004). These are expressed as in (Buckner et al., 2004; Raz et al., 2004): $Vol_{adj} = Vol - b(eICV - {}_{m}eICV)$. Vol_{adj} is the eICV

adjusted volume, Vol is the original uncorrected volume, b is the slope from the linear regression between Vol and eICV, eICV is the freesurfer derived intracranial volume for a participant and $_{m}$ eICV is the mean eICV across all participants. All multiple comparisons are reported using the Sidak correction.

3. Results

3.1. Behavioral Results from the N-Back Task

A multivariate ANOVA with N-Back task condition as the independent variable and D-prime and Reaction Time (RT) as dependent variables was conducted, controlling for age and gender. N-Back task condition was a significant main effect for both D-prime ($F(2,151) = 64.7$, SE = 0.25, $p < 0.0001$; partial $\eta^2 = 0.46$) and RT ($F(2,151) = 46.9$, SE = 24.3, $p < 0.0001$; partial $\eta^2 = 0.38$. Pair-wise comparisons (Sidak corrected) indicated that all task conditions were significantly different from each other on D-prime. Participants' had the highest D-prime score on the Compare condition (average D-prime = 6.12), followed by the 1-Back (average D-prime = 4.34; $p < 0.0001$) and then the 2-Back conditions (average D-prime = 2.19, $p < 0.0001$). D-prime was also significantly higher for the 1-Back than the 2-Back condition ($p < 0.0001$).

For RT, pair-wise comparisons (Sidak corrected) between the N-Back task conditions indicated that all three levels (Compare, 1-Back and 2-Back) significantly differed from each other. RTs were shortest during the Compare condition (771.35 ms) followed by the 1-Back (900.33 ms; $p < 0.0001$) and then the 2-Back conditions (1104.4 ms; $p < 0.0001$). Additionally, RTs were shorter during the 1-Back than the 2-Back condition ($p < 0.0001$).

3.2. fMRI N-Back Activation Results

Whole-brain activations associated with the 1-Back and 2-Back conditions were contrasted with activations during the Compare condition (1-Back/2 + 2-Back/2 > Compare) in order to localize the overall network of brain regions supporting visual working memory. Activation maps were thresholded at qFDR < 0.01 and all positively active regions (activity stronger for the N-Back than the Compare condition) from this contrast are shown in Fig. 3 and listed on Table 2. The center of mass coordinates from all the positively active regions (Table 2) were used as inputs to the Neurosynth database (Yarkoni et al., 2011) and these overlapped substantially with the core working memory network identified in previous studies from a meta-analysis sample of 1,091 working memory related articles included in the database. These positive, task-relevant activations included bilateral portions of the dorsolateral prefrontal cortex (DLPFC; Neurosynth meta-analytic coactivation r = 0.44), ventrolateral prefrontal cortex (VLPFC; Neurosynth meta-analytic coactivation r = 0.4), anterior cingulate cortex (ACC; Neurosynth meta-analytic coactivation r = 0.52) and inferior parietal lobule (IPL; Neurosynth meta-analytic coactivation r = 0.44).

Table 2. Brain Regions showing positive activation for the functional contrast of 1-Back/2 + 2-Back/2 > Compare. The table lists all positively active brain regions from the functional contrast of 1-Back/2 + 2-Back/2 > Compare, corresponding hemisphere, area (in number of voxels) and MNI center of mass coordinates.

3.3. Relationship between tFC and D-Prime

Results from the bootstrapped linear regression model indicated a significant positive association between average tFC (averaged across all seed ROIs, per participant) and log D-prime (bootstrapped Beta = 0.83, p = 0.033; SE = 0.38; 95% BCa CI = 0.164 to 1.5; Fig. 4), after controlling for age, gender and GCOR.

3.4. Relationship between Cortical QSM and D-prime

A bootstrapped linear regression model was used to evaluate the relationship between cortical GM QSM values in each lobe and log D-prime. The results indicated that parietal QSM was a significant predictor of log D-prime (bootstrapped Beta = −0.136, p = 0.009; SE = 0.049; 95% BCa CI = −0.24 to −0.05; VIF = 1.25; Fig. 5) after controlling for cortical GM CBF, adjusted total cortical GM volume, age and gender. That is, greater iron concentration in the parietal lobe was associated with poorer working memory performance. QSM in the other lobes did not predict working memory performance ($p_s > 0.3$; max VIF = 1.53). Adjusted total cortical GM volume was not a significant predictor of log D-prime (bootstrapped Beta = 1.46×10^{-7}, p = 0.67; SE = 3.2×10^{-7}; 95% BCa CI = -4.56×10^{-7} to 9.7×10^{-7}; VIF = 1.69).

3.5. Relationships between Cortical GM QSM and Cortical GM Volumes

Cortical GM QSM values from each lobe were not significant predictors of their corresponding cortical GM volumes or total cortical GM volume when controlling for corresponding cortical GM CBF, eICV, age and gender (Table 3). The results did not change when the Sidak multiple comparisons correction was removed, with none of the lobar-based predictors approaching uncorrected significance.

Table 3. Relationship between cortical QSM and corresponding cortical GM volume. The table illustrates the results of the bootstrapped linear regression analyses between total cortical, frontal, parietal, occipital and temporal lobe QSM values against corresponding cortical GM volume.

3.6. Relationship between cortical GM QSM and cortical GM CBF

The correlation between average cortical GM QSM and average cortical GM CBF was not significant, controlling for age, gender and eICV (bootstrapped Beta = −0.026, p = 0.12; SE = 0.017; 95% BCa CI = −0.054 to 0.014; $r^2 = 0.05$).

3.7. Relationship between Cortical GM QSM and tFC

This relationship was explored in a bootstrapped linear regression model with QSM values from each lobe as factors and average tFC (averaged across all seed ROIs) as the dependent variable. Results from the linear regression model indicated that lobar QSM was negatively associated with average tFC in the parietal mask (parietal QSM: 3.5 ppb/mm^3; bootstrapped Beta = −0.045, p = 0.005; SE = 0.015; 95% BCa CI = −0.073 to −0.025; VIF = 1.25; Fig. 6) after controlling for cortical GM CBF, adjusted cortical GM volume, age, gender and GCOR. QSM values from the other lobar masks were not significant predictors of average tFC ($p_s > 0.38$; max VIF = 1.55). Additionally, neither adjusted total cortical GM volume

nor total cortical GM CBF predicted average tFC in this model (cortical GM volume: bootstrapped Beta = 0.007, p = 0.40; SE = 0.009 95% BCa CI = −0.01 to 0.03; VIF = 1.69; cortical GM CBF: bootstrapped Beta = 0.0001, p = 0.88; SE = 0.002 95% BCa CI = −0.004 to 0.005; VIF = 1.37).

To decompose the negative association between parietal lobe QSM and average tFC, we conducted a bootstrapped multivariate linear regression between tFC from each seed ROI as multiple dependent variables and parietal QSM values as the main factor. Homologous tFC ROIs were merged across hemispheres to avoid issues of multicollinearity and to also reduce the number of dependent variables in the model. Parietal lobe GM CBF and adjusted parietal lobe GM volume were added as covariates, together with age, gender and GCOR.

Parietal lobe QSM was negatively associated with tFC in the VLPFC ROI (bootstrapped Beta = −0.044, p = 0.008; SE = 0.016; 95% BCa CI = −0.076 to −0.011) and the IPL ROI (bootstrapped Beta = −0.09, p < 0.0001; SE = 0.022; 95% BCa CI = −0.134 to −0.045; Fig. 7). Parietal lobe QSM did not predict tFC of the DLPFC ROI (bootstrapped Beta = −0.009, p = 0.52; SE = 0.015; 95% BCa CI = −0.04 to 0.019) or the ACC ROI (bootstrapped Beta = 0.004, p = 0.78; SE = 0.016; 95% BCa CI = −0.03 to 0.03) seed ROIs. Importantly, parietal lobe GM volume and parietal lobe GM CBF did not predict tFC in any of the seed ROIs (Parietal lobe GM volume p_s = 0.23; parietal lobe CBF ps = 0.16).

3.8. QSM Differences Between tFC Seed ROIs

The previous analyses indicated that parietal lobe QSM was negatively associated with tFC in the IPL and VLPFC ROIs but not the other ROIs. Subsequent analyses were thus conducted to determine if IPL and VLPFC ROIs showed higher QSM values than the other tFC ROIs. Age, gender and cortical GM CBF were added as covariates in the ANOVA. The omnibus ANOVA results indicated significant QSM differences between the tFC seed ROIs ($F(5,211) = 17.1$, $p < 0.0001$; partial $\eta^2 = 0.18$; Fig. 8). Bootstrapped, post-hoc comparisons indicated that the IPL (2.92 ppb/mm^3; 20% of ROI voxels consist of pQSM) seed ROIs had significantly higher iron concentration than all other ROIs: ACC (0.72 ppb/mm^3; 5% of ROI voxels consist of pQSM; p < 0.0001; SE = 0.37; 95% BCa CI = 1.54 to 2.94), DLPFC (0.58 ppb/mm^3; 4.4% of ROI voxels consist of pQSM; p < 0.0001, SE = 0.35; 95% BCa CI = 1.72 to 3.04) and VLPFC (1.93 ppb/mm^3; 13.7% of ROI voxels consist of pQSM; p = 0.05; SE = 0.5; 95% BCa CI = −0.053 to 1.98). Similarly, the VLPFC ROIs had significantly higher iron concentration than the ACC (p = 0.006; SE = 0.41; 95% BCa CI = 0.49 to 2.0) and DLPFC (p = 0.002; SE = 0.39; 95% BCa CI = 0.69 to 2.14) seed ROIs. Finally, the ACC and DLPFC ROIs did not differ significantly in QSM values (p = 0.41; SE = 0.17; 95% BCa CI = −0.16 to 0.49).

3.9. SNR associated with QSM within the lobar GM masks

An additional control analysis was conducted in order to evaluate the signal-to-noise ratio (SNR) in cortical and subcortical GM ROIs (Fig. 9) that could influence the QSM measures in these regions. For each ROI, SNR was calculated separately for each of the eight echoes of a magnitude images, acquired using the 3D spoiled GRE sequence for QSM, and then averaged across echoes into a single average SNR measure for each ROI. SNR was

calculated by dividing the mean image intensity value within a GM ROI (frontal, parietal, occipital, temporal, caudate and putamen ROIs), by the standard deviation of the intensity values outside the head (image background).

A repeated measures ANOVA was conducted with anatomical structure as an independent variable (with six levels, corresponding to each ROI) and SNR as the dependent variable. Age and gender were controlled in this analysis. The results indicated anatomical structure as a significant main effect $F(5,51) = 9.05$, $p < 0.0001$. Pairwise comparisons, adjusted for multiple comparisons using Sidak, indicated the following: SNR in the parietal lobe was significantly stronger compared to SNR in the caudate ($p = 0.001$) but comparable to that of the putamen ($p = 0.985$). Additionally, SNR in the frontal lobe was significantly lower in comparison to all other ROIs ($p_s < 0.0001$). Lastly, SNR in the occipital lobe was higher than in all other ROIs ($p_s < 0.0001$). As such, with the exception of the frontal lobe, SNR of the GRE images used in the QSM pipeline is comparable between cortical and subcortical GM ROIs.

4. Discussion

Our results demonstrate that high cortical iron is associated with low functional connectivity in a network of brain regions supporting working memory performance in older adults. We first identified a task-relevant network in which strength of functional connectivity (tFC) was positively associated with working memory performance in healthy older adults. We then showed that high iron concentration within this task-relevant network negatively impacted tFC and working memory performance after controlling for both brain volume and cerebral blood flow. Our results suggest that non-heme-iron mediated disruption of functional brain systems may be an early marker of age-related declines in working memory.

A body of previous work has linked excess brain iron concentration in basal ganglia structures with reduced working memory performance in older adults (cross-sectional: Bartzokis et al., 2011; Darki et al., 2016; longitudinal: Daugherty et al., 2015) and subsequent atrophy in basal ganglia structures 2 years later (Daugherty et al., 2015) and up to 7 years later (Daugherty and Raz, 2016). More recently, cross-sectional studies have reported negative associations between striatal iron concentration and BOLD magnitude in frontostriatal regions (Kalpouzos et al., 2017; Rodrigue et al., 2020) and striatal resting state functional connectivity with the rest of the brain (Salami et al., 2018).

However, the impact of cortical iron concentration on cortical functional connectivity networks directly supporting task performance has not been demonstrated. To address this question, we first identified task-relevant working memory brain regions in our sample. According to the Neurosynth database (Yarkoni et al., 2011), these frontoparietal brain regions overlapped substantially with the working memory network identified in a meta-analysis of 1,091 studies (e.g. Pessoa et al., 2002; Mitchell, 2007; Chein et al., 2010; Rottschy et al., 2012). Of central relevance to the goals of our study, mean strength of tFC within this frontoparietal network was positively associated with in-scanner working memory accuracy, after controlling for potential response biases by using D-Prime.

We then explored the impact of QSM derived brain iron concentration on this task-relevant frontoparietal network supporting working memory performance. Results indicated that high QSM-based iron concentration in the parietal lobe was associated with poorer working memory task performance and lower mean tFC strength in the IPL with the rest of the frontoparietal network. Collectively, our findings suggest that iron concentration may interfere with the exchange of information within the task-relevant working memory network in older adults. In contrast, we found no significant relationships between cortical GM volume, working memory performance and/or tFC. Additionally, we found no relationship between QSM-derived cortical GM iron concentrations and cortical GM volumes, even at uncorrected significance levels. This pattern is consistent with a view that high cortical iron concentration may negatively affect brain functional networks independently of its potential neurodegenerative effects.

Our results are pertinent to the recent Free Radical Induced Energetic and Neural Decline in Senescence model (FRIENDS; Raz and Daugherty, 2018). The FRIENDS model holds that age-related alterations in iron sequestration and transport reduce mitochondrial bioenergetic processes, lowering energy available for metabolically expensive processes such as neurotransmission. The model suggests that non-heme, iron-mediated generation of reactive oxygen species may disrupt metabolic and functional brain systems prior to inducing neurodegenerative processes associated with shrinkage of brain structures. Our finding that excessive iron is associated with reduced functional network connectivity, but not regional brain volumes, is broadly consistent with predictions of the FRIENDS model.

Our results indicated that iron concentration in the parietal lobe predicted lower tFC and working memory performance. Results from our follow-up analyses revealed a plausible explanation for this finding: iron concentration was significantly higher in the IPL ROIs of the parietal lobe compared to prefrontal cortex ROIs (DLPFC, VLPFC and ACC) of the functional working memory network in our participant cohort. This finding is consistent with a view that increasing regional iron concentration is associated with increasing regional functional connectivity disruption with the rest of the task network.

However, the specific finding of higher iron concentration observed in the IPL compared to prefrontal ROIs should be considered preliminary: 1) SNR was significantly lower in the frontal lobe, compared to all other lobes, which could explain the lack of significant correlations between QSM in this region, tFC and working memory performance; 2) the tFC seed ROIs are defined functionally at a much lower resolution compared to the QSM data (approximately 6 mm isotropic after smoothing, motion correction etc). As such extracting QSM values from gray matter only areas within these seed ROIs is not as reliable as those extracted from the high resolution, gray matter segmented MEMPR images. The lower resolution of the tFC seed ROIs is the main reason we evaluated lobar GM QSM instead of QSM extracted from these seed ROIs. Nonetheless, there appears to be some evidence that iron concentration in the parietal lobe (and motor cortex) may be higher than in prefrontal regions (e.g. Hallgren & Sourander, 1958; Buijs et al., 2016; Betts et al., 2016). A systematic investigation of regional differences in cortical iron accumulation in relation to different cognitive process, is a topic of considerable future interest.

Strengths of our study include the direct linking of MRI functional connectivity patterns with in-scanner task performance, the demonstration that this functional relationship is negatively affected by iron concentration, the control for both cerebral blood volume and GM structural volume in our QSM-functional models, the use of statistically rigorous bootstrapping to reduce the risk of Type I errors and demonstration of comparable SNR related to QSM signal in cortical task-relevant regions as subcortical regions. Further, the use of the same Freesurfer-derived GM lobar masks for extracting QSM data, volumetric data and CBF data maximize the likelihood that our cross-modal MRI data were extracted from the same cortical regions.

Limitations of our study include that QSM is not a direct measure of iron concentration and can be affected to a lesser extent by the presence of other metals, as well as calcification (ferrocalcinosis). In addition, QSM cannot differentiate between non-heme and heme iron bound to deoxygenated hemoglobin in blood (e.g, Wang and Liu, 2015). To this end, differences in cerebral blood volume (as measured by CBF), may contribute to the QSM signal (e.g. Bianciardi et al., 2014; Balla et al., 2014). Importantly, however, it should be noted that lobar GM CBF measures were not correlated with the functional connectivity patterns in our data nor with lobar GM QSM values. Thus, any potential contribution of CBF to QSM signal is unlikely to contribute to the negative relationship we observed between QSM and functional connectivity. Further, inclusion of CBF as a covariate in our models did not affect our observed QSM-FC relationships. We also note that no causal inferences can be made between QSM-based iron concentration, tFC and/or working memory performance. A longitudinal version of this study would be better suited for causal inference and one is planned with the same participants in two years.

Further, it should be noted that non-heme iron concentration varies between cortical layers (e.g. Kwan et al., 2012; Bulk et al., 2018). However, the relatively large voxel size of our scans prevents us from making inferences relating to QSM signal from specific cortical layers in gray matter and their relative contributions to the QSM effects we report. Lastly, the current study had a modest sample size which might have affected our ability to detect smaller effects between QSM, tFC and working memory performance. Future studies with a larger sample size should be used to identify possible subtler effects.

In conclusion, our results indicate a potential functional anatomic basis for the negative effects of iron on working memory previously reported in the literature. Specifically, our findings suggest that excess cortical iron may interfere with coordinated information processing within the frontoparietal network supporting working memory performance in healthy older adults.

Supplementary Material

Refer to Web version on PubMed Central for supplementary material.

Acknowledgments

This work was supported by the National Institutes of Health (grant numbers NIA R01AG055449, NIA P30 AG028383 and NIGMS S10 OD023573). The content is solely the responsibility of the authors and does not

necessarily represent the official views of these granting agencies. The authors declare no competing financial interests. The authors thank Shoshana Bardach for help with participant recruitment and Beverly Meacham and Eric Foreman for assisting/conducting the MRI scans. We also thank Drs. Anders Anderson and Pascal Spincemaille and Yi Wang for helpful discussions.

References

Acosta-Cabronero J, Machts J, Schreiber S, Abdulla S, Kollewe K, Petri S, Spotorno N, Kaufmann J, Heinze H-J, Dengler R, Vielhaber S, Nestor PJ, 2018 Quantitative susceptibility MRI to detect brain iron in amyotrophic lateral sclerosis. Radiology 289, 195–203. [PubMed: 30040038]

Ayton S, Fazlollahi A, Bourgeat P, Raniga P, Ng A, Lim YY, Diouf I, Farquharson S, Fripp J, Ames D, Doecke J, Desmond P, Ordidge R, Masters CL, Rowe CC, Maruff P, Villemagne VL, Salvado O, Bush AI, 2017 Cerebral quantitative susceptibility mapping predicts amyloid-β-related cognitive decline. Brain 140, 2112–2119. [PubMed: 28899019]

Buckner RL, Head D, Parker J, Fotenos AF, Marcus D, Morris JC, Snyder AZ, 2004 A unified approach for morphometric and functional data analysis in young, old, and demented adults using automated atlas-based head size normalization: reliability and validation against manual measurement of total intracranial volume. NeuroImage 23, 724–738. [PubMed: 15488422]

Buijs M, Doan NT, van Rooden S, Versluis MJ, van Lew B, Milles J, van der Grond J, van Buchem MA, 2016 In vivo assessment of iron content of the cerebral cortex in healthy aging using 7-Tesla T2*-weighted phase imaging. Neurobiol. Aging 53, 20–26. [PubMed: 28199888]

Bulk M, Abdelmoula WM, Nabuurs RJA, van der Graaf LM, Mulders CWH, Mulder AA, Jost CR, Koster AJ, van Buchem MA, Natté R, Dijkstra J, van der Weerd L, 2018 Postmortem MRI and histology demonstrate differential iron accumulation and cortical myelin organization in early- and late-onset Alzheimer's disease. Neurobiol. Aging 62, 231–242. [PubMed: 29195086]

Bartzokis G, Lu PH, Tingus K, Peters DG, Amar CP, Tishler TA, Finn JP, Villablanca P, Altshuler LL, Mintz J, Neely E, Connor JR, 2011 Gender and iron genes may modify associations between brain iron and memory in healthy aging. Neuropsychopharmacology 36, 1375–1384. [PubMed: 21389980]

Bianciardi M, van Gelderen P, Duyn JH, 2014 Investigation of BOLD fMRI resonance frequency shifts and quantitative susceptibility changes at 7 T. Hum. Brain Mapp 35, 2191–2205. [PubMed: 23897623]

Becerril-Ortega J, Bordji K, Fréret T, Rush T, Buisson A, 2014 Iron overload accelerates neuronal amyloid-β production and cognitive impairment in transgenic mice model of Alzheimer's disease. Neurobiol. Aging 35, 2288–2301. [PubMed: 24863668]

Behzadi Y, Restom K, Liau J, Liu TT, 2007 A component based noise correction method (CompCor) for BOLD and perfusion based fMRI. Neuroimage 37, 90–101. [PubMed: 17560126]

Balla DZ, Sanchez-Panchuelo RM, Wharton SJ, Hagberg GE, Scheffler K, Francis ST, Bowtell R, 2014 Functional quantitative susceptibility mapping (fQSM). NeuroImage 100, 112–124. [PubMed: 24945672]

Belleville S, Sylvain-Roy S, de Boysson C, Menard MC, 2008 Characterizing the memory changes in persons with mild cognitive impairment. Prog. Brain. Res 169, 365–375. [PubMed: 18394487]

Betts MJ, Acosta-Cabronero J, Cardenas-Blanco A, Nestor PJ, Düzel E, 2016 High-resolution characterisation of the aging brain using simultaneous quantitative susceptibility mapping (QSM) and R2* measurements at 7 T. Neuroimage 138, 43–63. [PubMed: 27181761]

Blacker D, Lee H, Muzikansky A, Martin EC, Tanzi R, McArdle JJ, Albert M, 2007 Neuropsychological measures in normal individuals that predict subsequent cognitive decline. Arch. Neurol 64, 862–871. [PubMed: 17562935]

Chein JM, Moore AB, Conway ARA, 2010 Domain-general mechanisms of complex working memory span. Neuroimage 54, 550–559. [PubMed: 20691275]

Chen G, Saad ZS, Britton JC, Pine DS, Cox RW, 2013 Linear mixed-effects modeling approach to FMRI group analysis. Neuroimage 73, 176–190. [PubMed: 23376789]

Cox RW, 1996 AFNI: software for analysis and visualization of functional magnetic resonance neuroimages. Comput. Biomed. Res 29, 162–173. [PubMed: 8812068]

Daugherty AM, Haacke EM, Raz N, 2015 Striatal iron content predicts its shrinkage and changes in verbal working memory after two years in healthy adults. J. Neurosci 35, 6731–6743. [PubMed: 25926451]

Daugherty AM, Raz N, 2016 Accumulation of iron in the putamen predicts its shrinkage in healthy older adults: A multi-occasion longitudinal study. Neuroimage 128, 11–20. [PubMed: 26746579]

Damoiseaux JS, Prater KE, Miller BL, Greicius MD, 2012 Functional connectivity tracks clinical deterioration in Alzheimer's disease. Neurobiol. Aging 33, 828.e19–828.e30.

Damoiseaux JS, 2017 Effects of aging on functional and structural brain connectivity. Neuroimage 160, 32–40. [PubMed: 28159687]

Darki F, Nemmi F, Möller A, Sitnikov R, Klingberg T, 2016 Quantitative susceptibility mapping of striatum in children and adults, and its association with working memory performance. Neuroimage 136, 208–214. [PubMed: 27132546]

Duncan NW, Wiebking C, Tiret B, Marjańska M, Hayes DJ, Lyttleton O, Northoff G, 2013 Glutamate concentration in the medial prefrontal cortex predicts resting-state cortical-subcortical functional connectivity in humans. PLoS One 8, e60312. [PubMed: 23573246]

Fukunaga M, Li TQ, van Gelderen P, de Zwart JA, Shmueli K, Yao B, …, Leapman RD, 2010 Layer-specific variation of iron content in cerebral cortex as a source of MRI contrast. Proc. Natl. Acad. Sci 107, 3834–3839. [PubMed: 20133720]

Glisky EL, 2007 Changes in cognitive function in human aging In: Riddle DR (Ed.), Brain aging: Models, methods, and mechanisms. Taylor & Francis Group, Boca Raton, pp. 3–20.

Gotts SJ, Saad ZS, Jo HJ, Wallace GL, Cox RW, Martin A, 2013 The perils of global signal regression for group comparisons: a case study of Autism Spectrum Disorders. Front. Hum. Neurosci 7.

Gotts SJ, Simmons WK, Milbury LA, Wallace GL, Cox RW, Martin A, 2012 Fractionation of social brain circuits in autism spectrum disorders. Brain 135 (9), 2711–2725. [PubMed: 22791801]

Grabner G, Janke AL, Budge MM, Smith D, Pruessner J, Collins DL, 2006 Symmetric atlasing and model based segmentation: an application to the hippocampus in older adults In: Lecture Notes in Computer Science (including subseries Lecture Notes in Artificial Intelligence and Lecture Notes in Bioinformatics). Springer Verlag, pp. 58–66.

Greicius MD, Kimmel DL, 2012 Neuroimaging insights into network-based neurodegeneration. Curr. Opin. Neurol 25, 727–734. [PubMed: 23108250]

Hallgren B, Sourander P, 1958 The effect of age on the non -haemin iron in the human brain. J Neurochem 3, 41–51. [PubMed: 13611557]

Hakun JG, Johnson NF, 2017 Dynamic range of frontoparietal functional modulation is associated with working memory capacity limitations in older adults. Brain Cogn 118, 128–136. [PubMed: 28865310]

Hametner S, Endmayr V, Deistung A, Palmrich P, Prihoda M, Haimburger E, Menard C, Feng X, Haider T, Leisser M, Köck U, Kaider A, Höftberger R, Robinson S, Reichenbach JR, Lassmann H, Traxler H, Trattnig S, Grabner G, 2018 The influence of brain iron and myelin on magnetic susceptibility and effective transverse relaxation - a biochemical and histological validation study. Neuroimage 179, 117–133. [PubMed: 29890327]

Hare DJ, Double KL, 2016 Iron and dopamine: a toxic couple. Brain 139, 1026–1035. [PubMed: 26962053]

Hentze MW, Muckenthaler MU, Andrews NC, 2004 Balancing acts: molecular control of mammalian iron metabolism. Cell 117, 285–297. [PubMed: 15109490]

Jenkinson M, Beckmann CF, Behrens TE, Woolrich MW, Smith SM, 2012 Fsl. Neuroimage 62, 782–790. [PubMed: 21979382]

Jo HJ, Saad ZS, Simmons WK, Milbury LA, Cox RW, 2010 Mapping sources of correlation in resting state FMRI, with artifact detection and removal. Neuroimage 52 (2), 571–582. [PubMed: 20420926]

Kagerer SM, van Bergen JM, Li X, Quevenco FC, Gietl AF, Studer S, …, van Zijl PC, 2020 APOE4 moderates effects of cortical iron on synchronized default mode network activity in cognitively healthy old-aged adults. Alzheimer's & dementia: diagnosis. Assess. Dis. Monit 12, e12002.

Kalpouzos G, Garzón B, Sitnikov R, Heiland C, Salami A, Persson J, Bäckman L, 2017 Higher striatal iron concentration is linked to frontostriatal underactivation and poorer memory in normal aging. Cereb. Cortex 27, 3427–3436. [PubMed: 28334149]

Kapogiannis D, Reiter DA, Willette AA, Mattson MP, 2013 Posteromedial cortex glutamate and GABA predict intrinsic functional connectivity of the default mode network. Neuroimage 64, 112–119. [PubMed: 23000786]

Kempton MJ, Underwood TSA, Brunton S, Stylios F, Schmechtig A, Ettinger U, Smith MS, Lovestone S, Crum WR, Frangou S, Williams SCR, Simmons A, 2011 A comprehensive testing protocol for MRI neuroanatomical segmentation techniques: evaluation of a novel lateral ventricle segmentation method. Neuroimage 58, 1051–1059. [PubMed: 21835253]

Kim HG, Park S, Rhee HY, Lee KM, Ryu CW, Rhee SJ, Lee SY, Wang Y, Jahng GH, 2017 Quantitative susceptibility mapping to evaluate the early stage of Alzheimer's disease. NeuroImage Clin 16, 429–438. [PubMed: 28879084]

Ke YA, Qian ZM, 2007 Brain iron metabolism: neurobiology and neurochemistry. Prog. Neurobiol 83, 149–173. [PubMed: 17870230]

Kwan JY, Jeong SY, van Gelderen P, Deng HX, Quezado MM, Danielian LE, Butman JA, Chen L, Bayat E, Russell J, Siddique T, Duyn JH, Rouault TA, Floeter MK, 2012 Iron accumulation in deep cortical layers accounts for MRI signal abnormalities in ALS: Correlating 7 tesla MRI and pathology. PLoS ONE 7 (4).

Langkammer C, Schweser F, Krebs N, Deistung A, Goessler W, Scheurer E, Sommer K, Reishofer G, Yen K, Fazekas F, Ropele S, Reichenbach JR, 2012 Quantitative susceptibility mapping (QSM) as a means to measure brain iron? a post mortem validation study. Neuroimage 62, 1593–1599. [PubMed: 22634862]

Lauffer RB, 1992 Iron, aging and human disease: historical background and new hypothesis In: Lauffer RB (Ed.), Iron and human disease. Taylor & Francis Group, Boca Raton, pp. 1–20.

Liu J, Liu T, De Rochefort L, Ledoux J, Khalidov I, Chen W, Tsiouris AJ, Wisnieff C, Spincemaille P, Prince MR, Wang Y, 2012 Morphology enabled dipole inversion for quantitative susceptibility mapping using structural consistency between the magnitude image and the susceptibility map. Neuroimage 59, 2560–2568. [PubMed: 21925276]

Liu T, Khalidov I, de Rochefort L, Spincemaille P, Liu J, Tsiouris AJ, Wang Y, 2011 A novel background field removal method for MRI using projection onto dipole fields. NMR Biomed 24, 1129–1136. [PubMed: 21387445]

Liu T, Liu J, de Rochefort L, Spincemaille P, Khalidov I, Ledoux JR, Wang Y, 2011b Morphology enabled dipole inversion (MEDI) from a single-angle acquisition: comparison with COSMOS in human brain imaging. Magn. Reson. Med 66, 777–783. [PubMed: 21465541]

Liu T, Surapaneni K, Lou M, Cheng L, Spincemaille P, Wang Y, 2012 Cerebral microbleeds: burden assessment by using quantitative susceptibility mapping. Radiology 262, 269–278. [PubMed: 22056688]

Liu T, Eskreis-Winkler S, Schweitzer AD, Chen W, Kaplitt MG, Tsiouris AJ, Wang Y, 2013 Improved subthalamic nucleus depiction with quantitative susceptibility mapping. Radiology 269, 216–223. [PubMed: 23674786]

Li W, Wu B, Batrachenko A, Bancroft-Wu V, Morey RA, Shashi V, Langkammer C, De Bellis M, Ropele S, Song W, Liu C, 2014 Differential developmental trajectories of magnetic susceptibility in human brain gray and white matter over the lifespan. Hum. Brain Mapp 35, 2698–2713. [PubMed: 24038837]

Matak P, Matak A, Moustafa S, Aryal DK, Benner EJ, Wetsel W, Andrews NC, 2016 Disrupted iron homeostasis causes dopaminergic neurodegeneration in mice. Proc Natl Acad Sci U S A 113, 3428–3435. [PubMed: 26929359]

Mills E, Dong XP, Wang F, Xu H, 2010 Mechanisms of brain iron transport: insight into neurodegeneration and CNS disorders. Futur. Med. Chem 2, 51–64.

Mitchell RL, 2007 fMRI delineation of working memory for emotional prosody in the brain: commonalities with the lexico-semantic emotion network. Neuroimage 36, 1015–1025. [PubMed: 17481919]

Moos T, Nielsen TR, Skjørringe T, Morgan EH, 2007 Iron trafficking inside the brain. J Neurochem 103, 1730–1740. [PubMed: 17953660]

Morris JC, Weintraub S, Chui HC, Cummings J, DeCarli C, Ferris S, Foster NL, Galasko D, Graff-Radford N, Peskind ER, Beekly D, Ramos EM, Kukull WA, 2006 In: The Uniform Data Set (UDS): Clinical and Cognitive Variables and Descriptive Data From Alzheimer Disease Centers, 20(4). Alzheimer Disease & Associated Disorders, pp. 210–216. doi: 10.1097/01.wad.0000213865.09806.92. [PubMed: 17132964]

Nasreddine ZS, Phillips NA, Bédirian V, Charbonneau S, Whitehead V, Collin I, Cummings JL, Chertkow H, 2005 The montreal cognitive assessment, MoCA: a brief screening tool for mild cognitive impairment. J. Am. Geriatr. Soc 53, 695–699. [PubMed: 15817019]

Park DC, Hedden T, 2001 Working memory and aging In: Naveh-Benjamin M, Moscovitch HL, Roediger HL (Eds.), Perspectives on human memory and cognitive aging: Essays in honour of Fergus Craik. Taylor and Francis Group, New York, pp. 148–160.

Penke L, Valdés Hernandéz MC, Maniega SM, Gow AJ, Murray C, Starr JM, Bastin ME, Deary IJ, Wardlaw JM, 2012 Brain iron deposits are associated with general cognitive ability and cognitive aging. Neurobiol. Aging 33, 510–517. [PubMed: 20542597]

Pessoa L, Gutierrez E, Bandettini P, Ungerleider L, 2002 Neural correlates of visual working memory: fMRI amplitude predicts task performance. Neuron 35, 975–987. [PubMed: 12372290]

Raz N, Gunning-Dixon F, Head D, Rodrigue KM, Williamson A, Acker JD, 2004 Aging, sexual dimorphism, and hemispheric asymmetry of the cerebral cortex: replicability of regional differences in volume. Neurobiol Aging 25, 377–396. [PubMed: 15123343]

Raz N, Daugherty AM, 2018 Pathways to brain aging and their modifiers: Free-radical-induced energetic and neural decline in senescence (FRIENDS) model-a mini-review. Gerontology 64, 49–57. [PubMed: 28858861]

Reuter-Lorenz PA, Sylvester CYC, 2005 The cognitive neuroscience of working memory and aging In: Cabeza R, Nyberg L, Park D (Eds.), Cognitive neuroscience of aging: Linking cognitive and cerebral aging. Oxford UP, New York, pp. 186–217.

Rodrigue KM, Daugherty AM, Haacke EM, Raz N, 2012 The role of hippocampal iron concentration and hippocampal volume in age-related differences in memory. Cereb Cortex 23, 1533–1541. [PubMed: 22645251]

Rodrigue KM, Daugherty AM, Foster CM, Kennedy KM, 2020 Striatal iron content is linked to reduced fronto-striatal brain function under working memory load. NeuroImage 210, 116544. [PubMed: 31972284]

Rottschy C, Langner R, Dogan I, Reetz K, Laird AR, Schulz JB, Fox PT, Eickhoff SB, 2012 Modelling neural correlates of working memory: a coordinate-based meta-analysis. Neuroimage 60, 830–846. [PubMed: 22178808]

Saad ZS, Reynolds RC, Jo HJ, Gotts SJ, Chen G, Martin A, Cox RW, 2013 Correcting brain-wide correlation differences in resting-state FMRI. Brain Connect 3, 339–352. [PubMed: 23705677]

Salami A, Avelar-Pereira B, Garzón B, Sitnikov R, Kalpouzos G, 2018 Functional coherence of striatal resting-state networks is modulated by striatal iron content. Neuroimage 183, 495–503. [PubMed: 30125714]

Sanfilipo MP, Benedict RHB, Zivadinov R, Bakshi R, 2004 Correction for intracranial volume in analysis of whole brain atrophy in multiple sclerosis: The proportion vs. residual method. NeuroImage 22, 1732–1743. [PubMed: 15275929]

Schmitt FA, Nelson PT, Abner E, Scheff S, Jicha GA, Smith C, Cooper G, Mendiondo M, Danner DD, Van Eldik LJ, Caban-Holt A, Lovell MA, Kryscio RJ, 2012 University of Kentucky Sanders-Brown healthy brain aging volunteers: donor characteristics, procedures and neuropathology. Curr. Alzheimer Res 9, 724–733. [PubMed: 22471862]

Smith SM, Jenkinson M, Woolrich MW, Beckmann CF, Behrens TEJ, Johansen-Berg H, Bannister PR, De Luca M, Drobnjak I, Flitney DE, Niazy RK, Saunders J, Vickers J, Zhang Y, De Stefano N, Brady JM, Matthews PM, 2004 Advances in functional and structural MR image analysis and implementation as FSL. Neuroimage 23, S208–S219. [PubMed: 15501092]

Stanislaw H, Todorov N, 1999 Calculation of signal detection theory measures. Behav. Res. Methods, Instrum., Comput 31, 137–149. [PubMed: 10495845]

Sullivan EV, Adalsteinsson E, Rohlfing T, Pfefferbaum A, 2009 Relevance of iron deposition in deep gray matter brain structures to cognitive and motor performance in healthy elderly men and women: Exploratory findings. Brain Imaging Behav 3, 167–175. [PubMed: 20161183]

Sun H, Walsh AJ, Lebel RM, Blevins G, Catz I, Lu JQ, Johnson ES, Emery DJ, Warren KG, Wilman AH, 2015 Validation of quantitative susceptibility mapping with Perls' iron staining for subcortical gray matter. Neuroimage 105, 486–492. [PubMed: 25462797]

Stoddard J, Gotts SJ, Brotman MA, Lever S, Hsu D, Zarate C, Ernst M, Pine DS, Leibenluft E, 2016 Aberrant intrinsic functional connectivity within and between corticostriatal and temporal–parietal networks in adults and youth with bipolar disorder. Psychol Med 46, 1509–1522. [PubMed: 26924633]

Taylor PA, Saad ZS, 2013 FATCAT: (an efficient) functional and tractographic connectivity analysis toolbox. Brain Connect 3, 523–535. [PubMed: 23980912]

Todorich B, Pasquini JM, Garcia CI, Paez PM, Connor JR, 2009 Oligodendrocytes and myelination: the role of iron. Glia 57, 467–478. [PubMed: 18837051]

Van Bergen JMG, Li X, Quevenco FC, Gietl AF, Treyer V, Meyer R, Buck A, Kaufmann PA, Nitsch RM, van Zijl PCM, Hock C, Unschuld PG, 2018 Simultaneous quantitative susceptibility mapping and Flutemetamol-PET suggests local correlation of iron and β-amyloid as an indicator of cognitive performance at high age. Neuroimage 174, 308–316. [PubMed: 29548847]

Van der Kouwe AJW, Benner T, Salat DH, Fischl B, 2008 Brain morphometry with multiecho MPRAGE. Neuroimage 40, 559–569. [PubMed: 18242102]

Wang Y, Liu T, 2015 Quantitative susceptibility mapping (QSM): decoding MRI data for a tissue magnetic biomarker. Magn. Reson. Med 73, 82–101. [PubMed: 25044035]

Wang Y, et al., 2017 Clinical quantitative susceptibility mapping (QSM): Biometal imaging and its emerging roles in patient care. J. Magn. Reson. Imaging 46, 951–971. [PubMed: 28295954]

Wayne Martin WR, Ye FQ, Allen PS, 1998 Increasing striatal iron content associated with normal aging. Mov. Disord 13, 281–286. [PubMed: 9539342]

Wisnieff C, Ramanan S, Olesik J, Gauthier S, Wang Y, Pitt D, 2015 Quantitative susceptibility mapping (QSM) of white matter multiple sclerosis lesions: Interpreting positive susceptibility and the presence of iron. Magn. Reson. Med 74, 564–570. [PubMed: 25137340]

Yarkoni T, Poldrack RA, Nichols TE, Van Essen DC, Wager TD, 2011 Large-s-cale automated synthesis of human functional neuroimaging data. Nat. Methods 8, 665–670. [PubMed: 21706013]

Zacks RT, Hasher L, Li KZH, 2000 Human memory In: Craik FIM, Salthouse TA (Eds.), The handbook of aging and cognition. Erlbaum, Mahwah, NJ, pp. 293–357.

Zecca L, Youdim MBH, Riederer P, Connor JR, Crichton RR, 2004 Iron, brain ageing and neurodegenerative disorders. Nat. Rev. Neurosci 5, 863–873. [PubMed: 15496864]

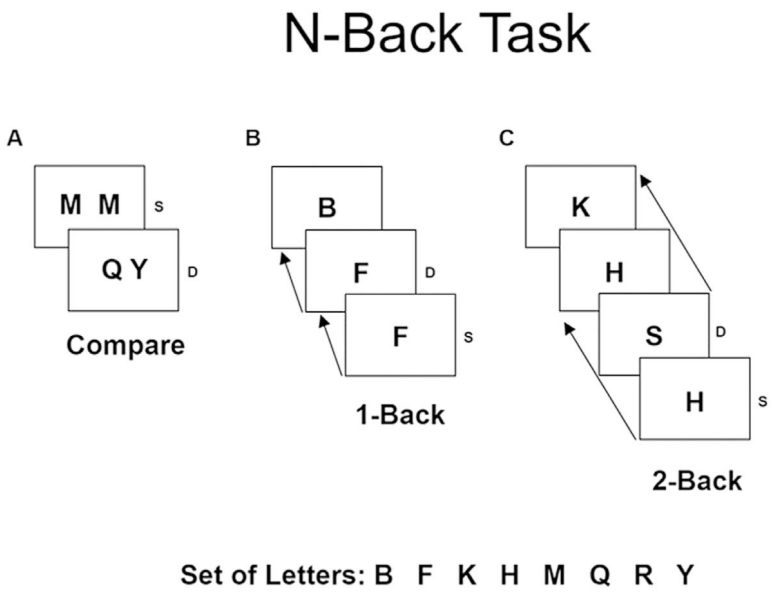

Fig. 1.

Example stimuli and sample trials from the N-Back task. The letter “S” next to trial panels indicates match trials in which a “same” response was required while the letter “D” appearing next to trial panels depicts a non-match trial in which a “different” response was required. A. Example trial displays from the Compare, visual control condition. B. Example trial displays from the 1-Back condition. C. Example trial displays from the 2-Back condition.

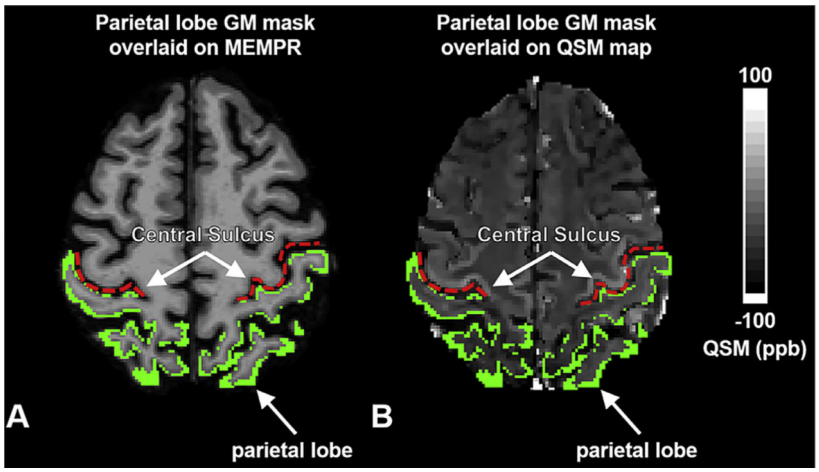

Fig. 2.

Lobar cortical GM masks for QSM. A representative example of a single participant's Freesurfer segmented parietal lobe cortical mask (in green) overlaid on their MEMPR image (A) and their QSM image (B). The QSM image depicts iron concentration in parts per billion (ppb) relative to CSF. Brighter areas on the QSM image have more iron concentration than CSF and darker areas less iron concentration than CSF (scaled between - 100 to 100 ppb). The rostral boundary of the parietal lobe mask (central sulcus) is indicated with a dashed red line to highlight the anatomical correspondence of GM structures captured by the mask across image modalities.

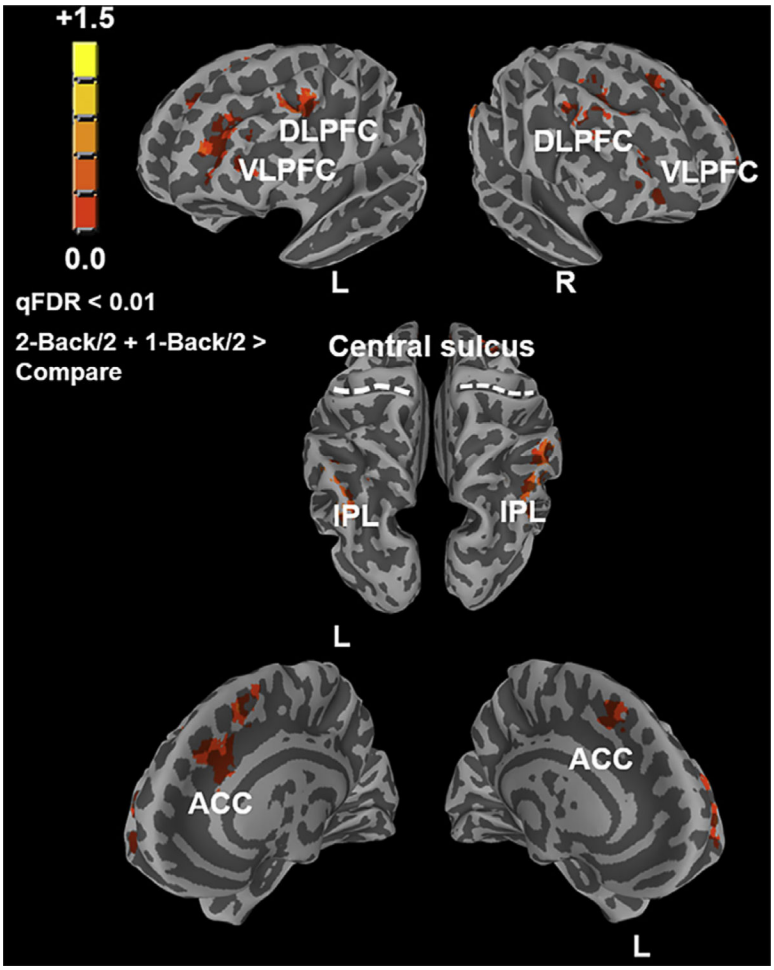

Fig. 3.

N-Back task activation map. The activation map reflects the voxelwise functional contrast of 2-Back/2 + 1-Back/2 > Compare. Positive activations (yellow-orange) indicate regions showing higher average N-Back activity than the control task. The 3D cortical meshes shown were created from the MNI ICBM152, 1 mm, 6th generation atlas using Freesurfer 6 and were partially inflated to aid identification of activations within sulci. Notes: ACC: Anterior cingulate cortex; DLPFC: Dorsolateral prefrontal cortex; VLPFC: ventrolateral prefrontal cortex; IPL: Inferior parietal lobule. The central sulci are demarcated (dashed white lines) to aid visual localization.

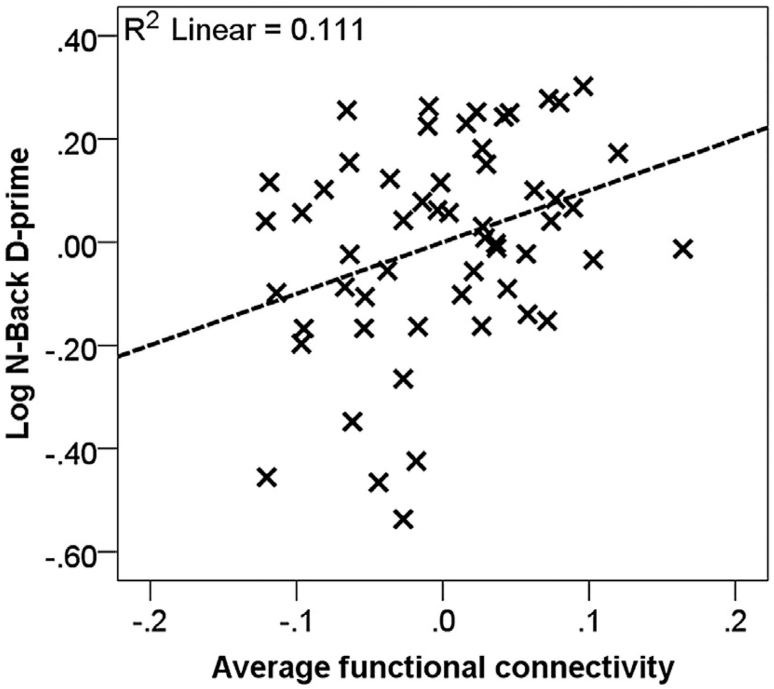

Fig. 4.

The relationship between N-Back performance and functional connectivity. The scatter plot depicts average task-based functional connectivity against performance (log D-prime, averaged across the 1-Back and 2-Back conditions of the N-Back task). Values are standardized residuals after controlling for age, gender and GCOR. The dashed line represents the linear best fit.

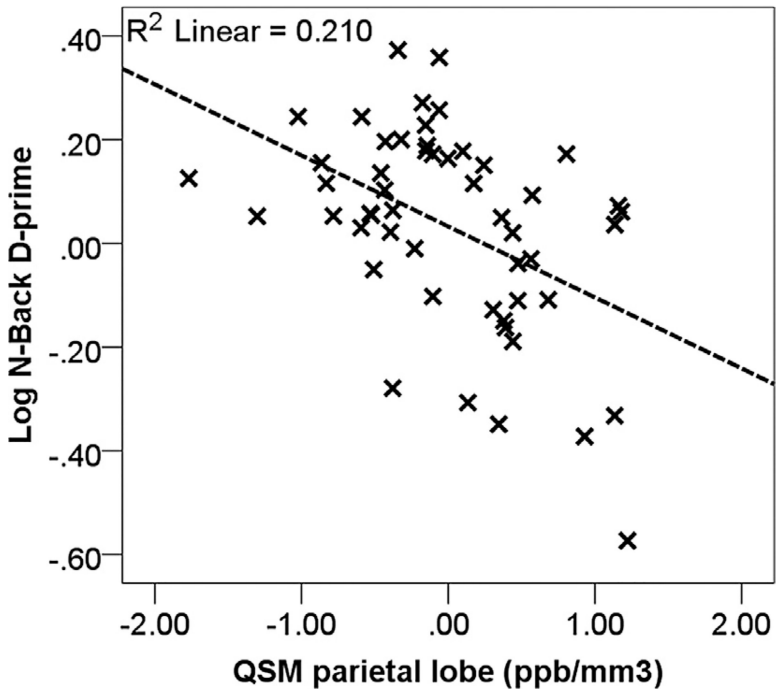

Fig. 5.

The relationship between parietal lobe QSM and performance. The scatter plot shows QSM parietal lobe values (iron concentration in ppb/mm^3) against N-Back task performance (log D-prime, averaged across the 1-Back and 2-Back conditions). Values are standardized residuals after controlling for age, gender, cortical GM CBF and adjusted cortical GM volume. The dashed line represents the linear best fit.

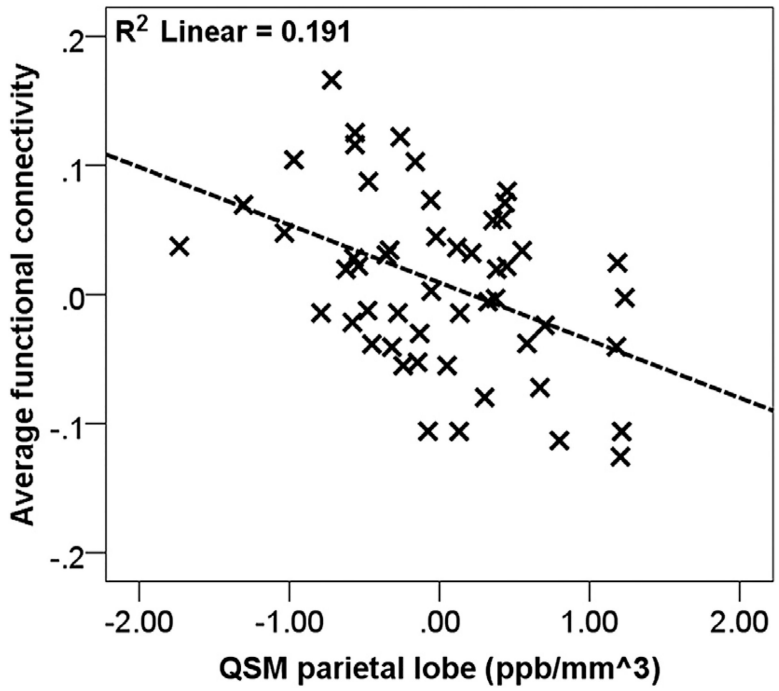

Fig. 6.

The relationship between average tFC and parietal lobe QSM. The plot shows average tFC (averaged across all seed ROIs) against QSM from the parietal lobe (iron concentration in ppb/mm^3). Values are standardized residuals after controlling for age, gender, GCOR, cortical GM CBF and adjusted cortical GM volume. The dashed line represents the linear best fit.

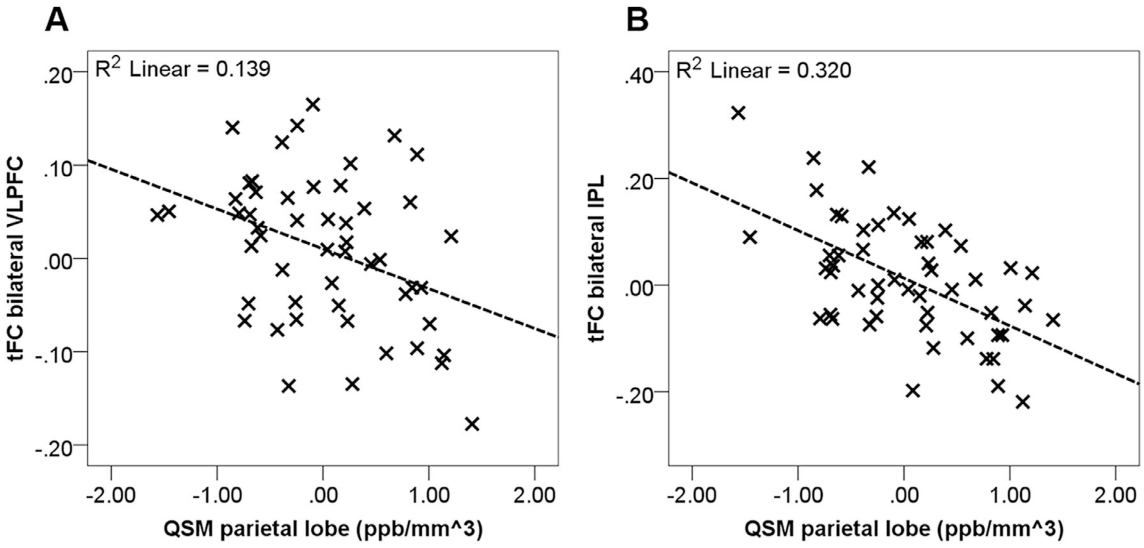

Fig. 7.

The relationship between QSM in the parietal lobe and average tFC from the VLPFC and IPL seed ROIs. The figure depicts parietal lobe QSM (iron concentration in ppb/mm^3) against average tFC from A. bilateral VLPFC and B. bilateral IPL seed ROIs (tFC between these seeds and every other seed ROI in the network). Values are standardized residuals after controlling age, gender, GCOR, parietal lobe GM CBF and adjusted parietal lobe GM volume. The dashed line represents the linear best fit.

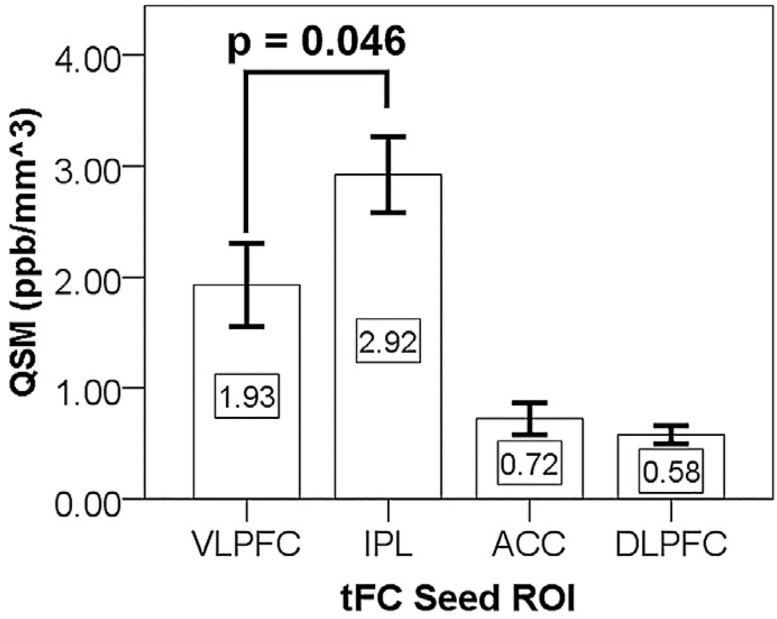

Fig. 8.

Iron concentration for each tFC seed ROI merged across hemispheres. The bar chart depicts QSM (iron concentration in ppb/mm^3) for the VLPFC, IPL, ACC and DLPFC seed ROIs. The error bars denote + /−1 standard error of the mean.

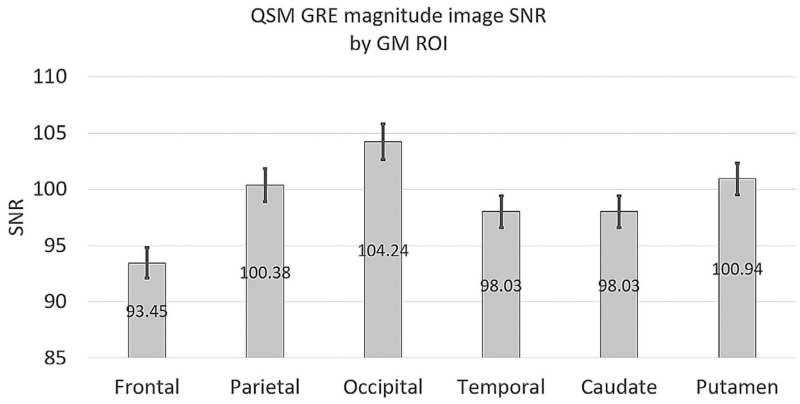

Fig. 9.

Average SNR for cortical and subcortical gray matter ROIs. SNR was calculated separately for each echo of a magnitude image, part of the 3D spoiled GRE sequence used for QSM. SNR from all echoes was then averaged together for each ROI, across participants. The error bars denote +/−1 standard error of the mean.

Table 1

Group Demographics and Mean Cognitive Measures

n	**55**
Age (years)	72.07 ± 5.32
M:F	24:31
Education (years)	16.51 ± 2.40
MMSE[1]	28.93 ± 1.26
MoCA[2]	26.67 ± 2.662

Mean ± standard deviation is shown for participants.

[1]MMSE: Mini-Mental State Exam, collected for 47 participants.

[2]MoCA: Montreal Cognitive Assessment, collected for 55 participants.

Table 2

Regions Showing Positive Activation for the Functional Contrast of 1-Back/2+2-Back/2 > Compare.

Hemisphere	Region	Cluster Size	X	Y	Z
L	Inferior Parietal Lobule (IPL)	80	−37	−69	46
R	Inferior Parietal Lobule	143	47	−55	45
L	Dorsolateral Prefrontal Cortex (DLPFC)	75	−44	23	37
R	Dorsolateral Prefrontal Cortex	120	36	27	39
L	Ventrolateral Prefrontal Cortex (VLPFC)	137	−31	52	11
R	Ventrolateral Prefrontal Cortex	30	32	−55	45
L	Anterior Cingulate Cortex (ACC)	31	−6	29	43
R	Anterior Cingulate Cortex	110	6	23	46

Cluster size is measured by number of voxels.

Coordinates are for the MNI center of mass.

Table 3

Relations between cortical GM QSM and corresponding cortical GM volume

Lobe	Bstrapped Beta/r^2	p	Std. Error	95% BCa CI
Total cortical	139.7/0.0009	0.83	611.3	−1252.1 to 1406.1
Frontal	−656.8/0.01	0.54	1055.2	−3030.8 to 1484.6
Parietal	−33.5/0.00003	0.97	975.6	−1909.6 to 1973.6
Occipital	−89.3/0.004	0.60	193.7	−498.5 to 437.2
Temporal	90.6/0.001	0.82	387.6	−659.7 to 720.8